Materials Science in Semiconductor Processing 92 (2019) 19–27

Contents lists available at ScienceDirect

Materials Science in Semiconductor Processing

journal homepage: www.elsevier.com/locate/mssp

High-performance germanium quantum dot photodetectors in the visible and near infrared

Stylianos Siontas[a,*], Dongfang Li[a], Haobei Wang[b], Aravind A.V.P.S[a], Alexander Zaslavsky[a,b], Domenico Pacifici[a,b]

[a] School of Engineering, Brown University, 184 Hope St., Providence, RI 02912, USA
[b] Department of Physics, Brown University, 182 Hope St., Providence, RI 02912, USA

ARTICLE INFO

Keywords:
Germanium
Quantum dot
Photodetector
Temperature
Near infrared

ABSTRACT

We present our work on high performance germanium (Ge) quantum dot (QD) photodetectors (PDs), fabricated on Si and Ge substrates, that operate via tunneling transport through a QD-containing active layer and feature high internal photoconductive gain. In the $\lambda = 400$–1100 nm range, the PDs fabricated on Si substrates exhibit room-temperature spectral responsivity (R_{sp}) up to 4 A/W and internal quantum efficiency (IQE) up to 700%. At $\lambda = 640$ nm and 12 μW of incident power, signal-to-noise ratio (SNR) of 7×10^6 and specific detectivity (D^*) of 1.2×10^{11} cmHz$^{1/2}$W^{-1} are obtained. The PDs demonstrate 3 dB bandwidths (f_{3dB}) up to 10 MHz, corresponding to response times of ~ 40 ns. When operated at 100 K temperature the performance improves, especially at low incident power, where at 10 nW D^* increases to 2×10^{13} cmHz$^{1/2}$W^{-1}, due to IQE in excess of 22000%. In order to extend the photoresponse into the near-infrared (near-IR), PDs were fabricated on Ge substrates, yielding room-temperature $R_{sp} = 1.5$ A/W, IQE = 134% and $f_{3dB} = 10$ kHz at the $\lambda = 1550$ nm telecommunication wavelength. Significant improvement to f_{3dB} is expected in PDs employing thinner QD-containing layers. Lowering temperature to 50 K and incident power to 10 nW yield $D^* = 10^{13}$ cmHz$^{1/2}$W^{-1}, resulting from IQE exceeding 60000%. Based on the above figures of merit, as well as their Si technology compatibility, our Ge QD PDs appear promising for high-performance photodetectors working in the visible and near-IR.

1. Introduction

Efficient photodetection of visible and near infrared light is crucial for technological applications such as fiber optic telecommunications, optical interconnects on chips and CMOS imaging cameras. Necessary attributes of a high performance photodetector (PD) are high photon to electron conversion efficiency, i.e., high responsivity (R_{sp}); ability to detect weak incident optical signals, i.e., high specific detectivity (D^*); high signal-to-noise ratio (SNR); and finally fast response time, i.e., ability for the photo-generated current to quickly follow the modulation of the optical signal. Commercial photodetectors employing the intrinsic photoelectric effect are fabricated using a variety of materials, commonly bulk semiconductors, including but not limited to silicon (Si), germanium (Ge) and indium gallium arsenide (InGaAs), depending on the wavelength detection range. However, such devices are known to have intrinsic limitations in their photo-conversion efficiencies as they do not exhibit gain unless operated in avalanche mode, which requires high-voltage biasing and slows the response time. On the other hand, significant advantages arise by shrinking the size of bulk materials down to the nanoscale in order to form zero-dimensional quantum dots (QDs). Specifically, semiconductor QDs are characterized by reduced phonon scattering, leading to longer carrier relaxation times which favors photoconductive gain, as well as confinement in all three spatial dimensions that can reduce the dark current, both contributing to higher SNR. Furthermore, QDs are characterized by a tunable bandgap which allows broad wavelength selection. Finally, intersubband transitions are polarization-independent, so normally incident optical signals can be detectable.

Quantum dot photodetectors have been fabricated employing a variety of active materials such as Si, Ge, InGaAs and PbS. Starting with Si, Shieh et al. [1,2] have shown that the incorporation of Si QDs in a SiO_2 matrix on silicon substrates successfully increased the PDs' IQE up to 200% and achieved $R_{sp} = 0.4$–2.8 A/W in the visible, thus beating the performance of a standard Si photodiode with peak responsivity not more than 0.7 A/W [3]. As for photodetectors based on Ge QDs dispersed within a SiO_2 matrix on silicon substrates, Hsu et al. [4] reported devices with responsivities of 0.13 A/W at $\lambda = 820$ nm, whereas Tzeng et al. [5] reported values up to 1.8 A/W with corresponding IQE up to 400% at

* Corresponding author.
E-mail address: stylianos_siontas@brown.edu (S. Siontas).

https://doi.org/10.1016/j.mssp.2018.03.024
Received 31 January 2018; Received in revised form 14 March 2018; Accepted 19 March 2018
Available online 07 April 2018
1369-8001/

$\lambda = 600$ nm. Finally, Cosentino et al. [6] reported PDs exhibiting an even further increase of IQE up to 1500%. Additionally, PDs based on solution-processed colloidal PbS QDs have showed high $R_{sp} = 1000$ A/W, D^* up to 1.8×10^{13} cmHz$^{1/2}$W^{-1} and bandwidths as high as 3 MHz for photodetection in the 800–2000 nm range [7–9]. As for photodetectors sensitive to mid and long-IR radiation, various groups have reported PDs employing stacks of InAs QDs within InGaAs quantum wells [10–13] with best performances reaching R_{sp} as high as 2.5 A/W at $\lambda = 10$ μm and T = 190 K [14] and $D^* = 3 \times 10^{11}$ cmHz$^{1/2}$W^{-1} at $\lambda = 9.3$ μm when cooled down to 78 K [15].

Here we present a review of our work on QD photodetectors based on Ge QDs embedded within a SiO_2 matrix, deposited on Si and Ge substrates for efficient photodetection in the visible and near-IR. The PDs exhibit high responsivity, detectivity and fast response times, and are fully compatible with silicon fabrication technology both in terms of substrate compatibility and in terms of the thermal budget, as they are characterized by lower synthesis temperatures than Si QDs [16,17]. Furthermore, Ge possesses a higher absorption coefficient, especially when embedded in a SiO_2 matrix due to localized interface states [18–20] and finally a larger excitonic Bohr radius compared to Si, which allows better modulation of the bandgap with QD size.

2. Fabrication process

In our fabrication procedure, Ge and SiO_2 targets were co-sputtered on *n*- and *p*-type Si or Ge substrates held at a temperature of 400 °C during deposition, yielding oxide matrix films of thicknesses $W_{QD} = 60$–230 nm with embedded Ge QDs (as measured by profilometry and ellipsometry). After deposition, the thickness could be further adjusted by etching in a dilute hydrofluoric acid (HF) solution. Transmission electron microscopy (TEM) showed the presence of small, densely and homogeneously distributed Ge QDs in the as-grown film with mean QD diameter of 3 nm [18,21]. Following deposition, some samples were annealed at 500 °C in a N_2 environment for 30 min thus generating larger size and more densely packed Ge QDs with improved crystalline quality [18] with the aim of providing devices with a broader and more uniform photoresponse [6]. Subsequently, an optically transparent, highly-conductive 55 or 100 nm (as measured by profilometry and ellipsometry) indium zinc oxide (IZO) or indium tin oxide (ITO) layer of resistivity ≤ 0.001 Ωcm (as measured by a four probe measurement) was sputter-deposited as the top electrode. Finally, photolithography was performed in order to define various active area devices, obtained by etching away the IZO or ITO and Ge QD/SiO_2 layers using a dilute HF solution, with the aim of suppressing leakage current on the unpassivated sidewall surface that is present in cleaved samples. The structure was completed with a silver paste or indium back contact and attaching to a glass or sapphire substrate [22,23]. The PD schematic cross-section is presented in Fig. 1 (a).

3. Room-temperature photoresponse

Current-voltage (*I–V*) measurements were carried out in the dark and under illumination as a function of incident wavelength. Two 1.5 mm^2 area detectors, with $W_{QD} = 200$ nm, both fabricated on *n*-type Si substrates that were annealed after deposition (see Section 2), one fabricated by cleaving the as-deposited substrate and the other defined by photolithography (see schematic in Fig. 1(a)), were illuminated at a representative incident $\lambda = 600$ nm at $P_{in} = 12$ μW of incident power. The *I–V* curves are plotted in Fig. 1 (b). The PDs rectify in the dark with a rectification ratio greater than three orders of magnitude, measured at symmetric voltages of −1 and 1 V and show a strong photoresponse (three orders of magnitude for the photolithographically defined sample) at −10 V. The photoresponse saturates for reverse bias higher than −5 V implying that they can be operated with almost unchanged performance in that range. Most importantly, it is observed that the device defined by photolithography shows an order of magnitude

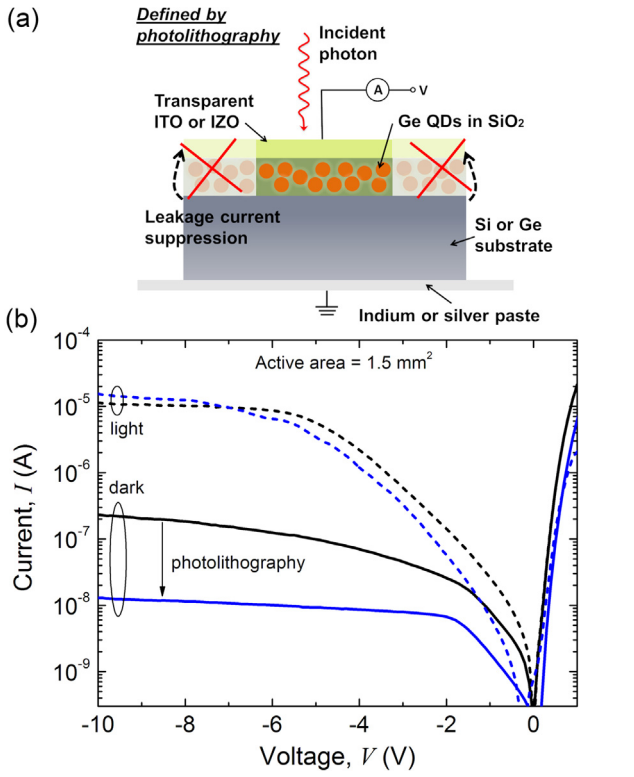

Fig. 1. (a) Schematic cross-section of a Ge QD PD. The active area is defined by photolithography in order to suppress peripheral leakage current (depicted by arrows) on the unpassivated sidewall surface which is present in devices defined by cleaving (depicted as semi-transparent). (b) Current-voltage characteristics showing the photoresponse of two 1.5 mm^2 PDs as a function of reverse bias, in the dark and under illumination of $\lambda = 600$ nm at $P_{in} = 12$ μW. Black/blue solid lines depict dark current of cleaved/photolithographically defined detectors, showing significant suppression of leakage current, whereas dashed lines show current under illumination. (Adapted from [23]).

decrease in dark current as a consequence of suppressed leakage (see Fig. 1(a)). An even lower dark current was observed when decreasing the device active area to 0.5 mm^2, with values down to 6×10^{-9} A (not shown).

The mean values and standard deviation (presented as error bars) of R_{sp} and internal quantum efficiency (IQE) of two pairs of identical area PDs with areas equal to 1.5 and 0.5 mm^2 are shown in Fig. 2 at a reverse bias of −10 V, together with the measured reflectance ($R(\lambda)$) at normal incidence, over the $\lambda = 400$–1100 nm wavelength range provided by a xenon lamp coupled to a spectrograph for individual wavelength selection. The responsivity in Fig. 2 (a) was measured by first calculating the photocurrent, i.e. $I_{ph} = |I_t - I_d|$, defined as the total current under illumination (I_t) minus the dark current (I_d) at the given reverse bias and incident wavelength, and dividing it by the incident optical power, P_{in}, i.e.

$$R_{sp}(\lambda) = \frac{I_{ph}(\lambda)}{P_{in}(\lambda)}. \quad (1)$$

As is evident in Fig. 2 (a), the mean R_{sp} of the 0.5 mm^2 devices reaches a maximum of ~ 2 A/W, whereas that of the 1.5 mm^2 devices is ~ 1.7 A/W. The responsivity drops off when approaching the near-UV as well as near-IR but it is still ~ 0.3 A/W at 400 nm and 1100 nm, i.e. near the band-edge of the Si substrate. This is in contrast to the results obtained by measuring the *I–V* curves of as-deposited (unannealed) samples with slightly larger thickness ($W_{QD} = 230$ nm) where R_{sp}, albeit possessing a higher peak value of 4 A/W at same reverse bias of −10 V, goes to zero when approaching the silicon bandgap (see Fig. 2(a)). The annealed devices exhibit a lower peak but a broader and more uniform

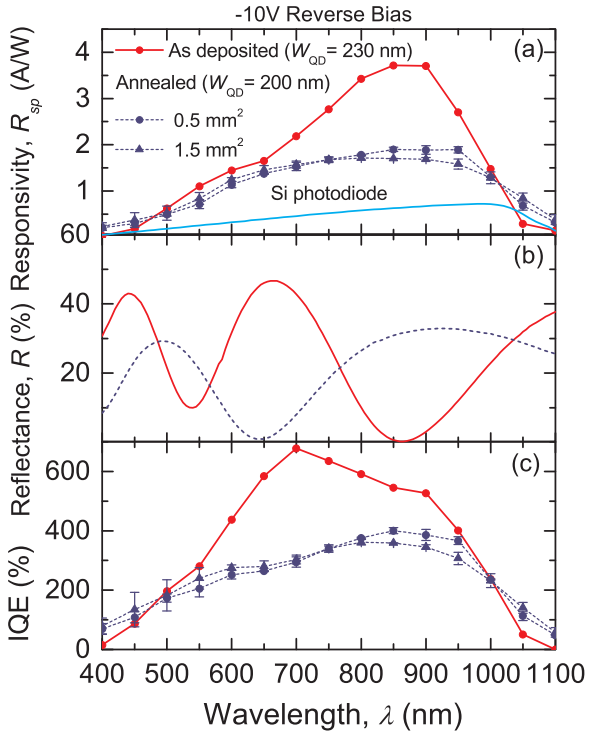

Fig. 2. (a) Spectral responsivity (R_{sp}), (b) Normal incidence reflectance (R) and (c) Internal quantum efficiency (IQE) spectra of as-deposited and annealed Ge QD PDs at reverse bias of −10 V. In panels (a) and (c), for the annealed samples, each point represents the mean value, whereas the error bars represent the standard deviation of measurements performed on different devices with same area. Light blue curve in panel (a) depicts R_{sp} of a standard Si photodiode [3]. (Adapted from [22,23]).

spectral photoresponse. The extended spectral response can be explained by increased Ge QD size associated with an amorphous to crystalline phase transition [18,24], leading to a smaller absorption bandgap, whereas absence of sharp absorption peaks is attributed to dispersion of QD sizes and an abundance of surface states [6]. Additionally, the low standard deviation of the mean R_{sp} for same area devices at all incident wavelengths is evidence that our fabrication process leads to reproducible results. Moreover, R_{sp} values show little dependence on active area as the incident power density was kept constant during the measurements. Most importantly the devices show much higher responsivity over the whole 400–1100 nm wavelength range compared to a conventional Si photodiode [3] as clearly seen in Fig. 2 (a), even when operated at lower bias voltage of –5 and −2 V (see [22] for details). The IQE as a function of λ was also calculated as follows:

$$\mathrm{IQE}(\lambda) = \frac{\mathrm{EQE}(\lambda)}{1 - R(\lambda)}. \tag{2}$$

where $R(\lambda)$ is the specular reflectance shown in Fig. 2 (b), in which the blue-shifting of the W_{QD} = 200 nm sample's reflectance peaks, compared to the W_{QD} = 230 nm sample originates from shorter wavelength modes supported within the respectively thinner optical cavity. Finally, EQE is the external quantum efficiency calculated by normalizing the photo-generated current by the number of incident photons at each wavelength, i.e.

$$\mathrm{EQE}(\lambda) = \frac{hc}{\lambda} R_{sp} \tag{3}$$

The results are summarized in Fig. 2 (c) for both unannealed samples, showing IQE as high as 700%, and annealed samples showing a lower peak value of 400%, but with a strong non-zero response near the Si band-edge, i.e. IQE ~ 50% at λ = 1100 nm for both 1.5 and 0.5 mm^2 detectors. The obtained values of IQE >100% throughout the λ = 450–1000 nm range are clear indication of an internal gain mechanism present in the devices. Since gain persists down to reverse bias as low as −2 V (see [22]) and an electron transverses more than 20 QDs in a W_{QD} ~ 100 nm layer, impact ionization can be ruled out as a dominant gain mechanism. Instead, our explanation for the high photoconductive gain of the PDs is as follows: 1) Electron-hole pairs are photogenerated both in the Ge QDs and in the substrate; 2) due to the large difference in the tunneling mass, the holes are exponentially slower than electrons to tunnel between QDs in the SiO_2; therefore 3) a net positive hole charge accumulates in the QD layer and, in order to maintain charge neutrality, 4) additional electrons need to be supplied from the IZO or ITO reservoir, which tunnel through the SiO_2 and contribute to the observed photocurrent. A similar gain mechanism has been suggested previously for photoconductive gain in QD PDs [4,25] as well as in QW PDs [26].

4. Room-temperature transient photoresponse

A systematic study of the response time as a function of illumination power, QD layer thickness (W_{QD}) and series load resistance (R_L) is presented in this section. All response time measurements were performed by illuminating the device, held at fixed reverse bias value of −2 V with a modulated diode laser (either by a mechanical chopper or by direct digital modulation of the laser) outputting light at λ = 670 nm. The photogenerated current was obtained by measuring the voltage drop across the load resistor R_L connected in series with the PD [27]. Starting with the rise time (τ_{on}), it consists of an intrinsic, optically induced turn-on time (directly linked to the optical excitation rate of electron-hole pairs in the QDs and in the silicon substrate) together with a contribution from the characteristic $\mathscr{R}$C time constant of the circuit, where $\mathscr{R}$ is the total of the load resistance R_L and intrinsic series resistance of the detector. To quantify these effects, the transient behavior of the photocurrent was measured under various illumination powers and R_L values. The dependence of τ_{on} on R_L, plotted at two incident optical power values, is presented in Fig. 3 for a W_{QD} = 230 nm detector. The inset shows the time-resolved normalized photocurrent from which τ_{on} is extracted, for the representative R_L = 10 kΩ case. As expected, τ_{on} decreases with R_L for a given incident optical power due to a smaller $\mathscr{R}$C time constant, with a minimum measured τ_{on} falling in the 1 − 2 μs range, fast compared to other reported QD-based PDs [28–30].

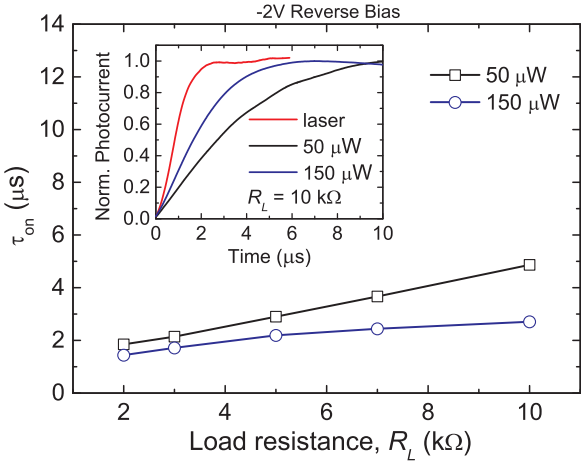

Fig. 3. Turn-on time (τ_{on}) vs. load resistance (R_L) at −2 V bias, at two different incident powers for a W_{QD} = 230 nm PD. The inset shows the time-resolved normalized photocurrent curves for R_L = 10 kΩ at two illumination powers. The red line represents the system response obtained by measuring the modulated laser beam using a fast commercial Si photodiode. (Reprinted with the permission of the American Institute of Physics.).

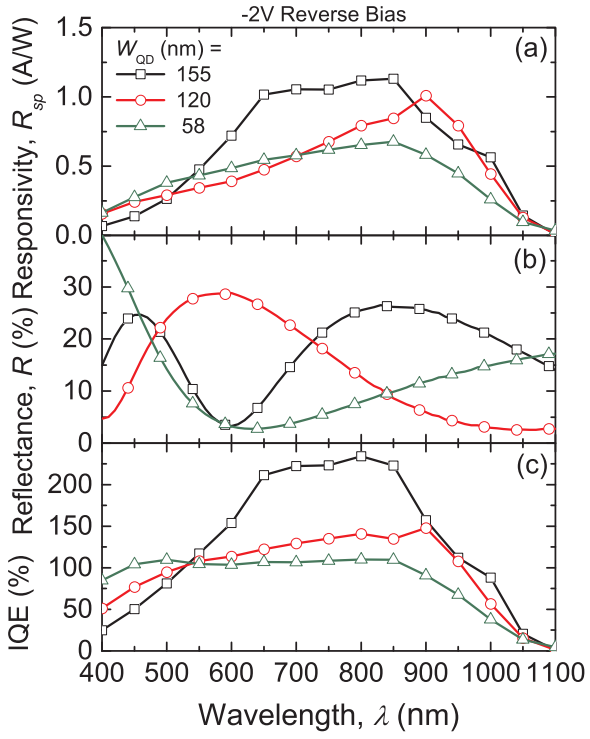

Fig. 4. (a) R_{sp}, (b) R and (c) IQE for devices of varying W_{QD} at −2 V of reverse bias. (Reprinted with the permission of the American Institute of Physics.).

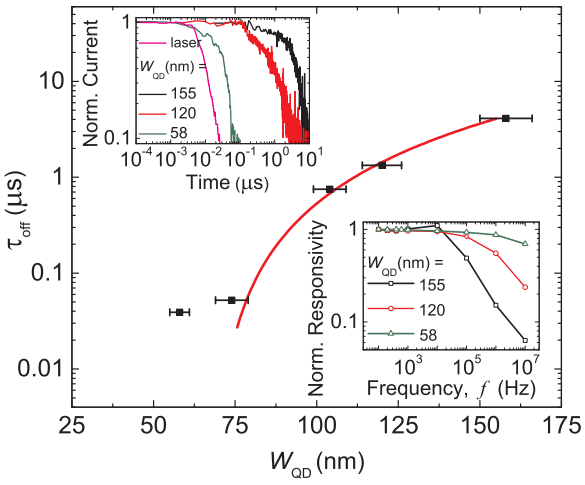

Fig. 5. Measured τ_{off} vs. W_{QD} (solid squares) and fit of the experimental data showing a quadratic dependence (red line). Top inset shows time-resolved normalized photocurrent response measured at −2 V bias and 2 mW incident power, using a 50 Ω load resistor. Bottom inset shows normalized responsivity vs. modulation frequency (f) for devices with W_{QD} = 155, 120 and 58 nm measured at the same conditions. All measurements were performed at λ = 670 nm illumination wavelength. (Reprinted with the permission of the American Institute of Physics.).

Moreover, Fig. 3 also shows that, for a given series resistance, faster turn-on times can be achieved by increasing the incident optical power, due to a higher excitation rate leading to an increased PD conductivity.

As for the turn-off time (τ_{off}), it is identified with the transit time of the electrons through the QD network and the electron-hole pair recombination time. Assuming one of the main delays comes from the transit time due to the diffusive percolative hopping of electrons tunneling between adjacent QDs, which to first approximation is proportional to W_{QD}^2, faster response times can be achieved by fabricating thinner devices. For this reason samples with various thinner active layers were fabricated by etching down the original 230 nm-thick films using a dilute HF solution [27]. The experimentally measured R_{sp}, R and IQE of three samples with varied W_{QD} = 155, 120 and 58 nm, are presented in Fig. 4 (a), (b) and (c). The three different W_{QD} values were estimated by fitting the reflectance curves of Fig. 4 (b) implementing a multiple reflection model that takes into account the optical constants of the various dielectric layers and modeling the QD layer using an effective medium approximation (EMA) where the Ge concentration was obtained by performing Rutherford backscattering spectrometry (RBS) (data not shown here). From Fig. 4 (a), it is evident that reducing W_{QD} only slightly reduces R_{sp}. Even for the thinnest W_{QD} ~ 60 nm PD, the IQE is roughly constant at ~ 100% over a wide λ = 400–850 nm range (see Fig. 4 (c)). On the other hand, τ_{off}, measured at bias of −2 V, using a 50 Ω series resistor and 2 mW of incident optical power, decreases quickly with W_{QD} as seen in Fig. 5, where the horizontal error bars demonstrate the error in estimating W_{QD} due to uncertainty of the Ge concentration value. The time-resolved data of the normalized photocurrent from which τ_{off} was exacted is provided in the top inset of Fig. 5. Reducing W_{QD} down to ~ 60 nm reduces τ_{off} to ~ 40 ns, at the cost of a slightly lower peak responsivity which is still above 0.5 A/W as is evident in Fig. 4 (a). In order to verify the proposed carrier diffusive hopping mechanism, the obtained response time data was quadratically fitted, as shown in Fig. 5. The fit is reasonably consistent with the measured data except at the lowest thickness value, where the deviation can be attributed to parasitic capacitance (see [27] for details). The fact that thinner PDs lead to faster response time, was also confirmed by performing roll-off measurements of the normalized responsivity as a function of laser modulation frequency (f) as is presented in the bottom inset of Fig. 5 for the three respective W_{QD} values. As can be seen, the responsivity of the 155 nm thick PD begins to fall off quickly corresponding to a 3 dB bandwidth (f_{3dB}) of 40 kHz. However, the 3 dB roll-off for the thinner devices can be pushed to higher frequencies as the result of the faster rise and decay times. Specifically, for the thinnest ~ 60 nm device, a f_{3dB} value of 10 MHz is achieved, corresponding to the τ_{off} ~ 40 ns value reported above. This suggests that even faster response times may be achievable by further reducing QD layer thickness. Finally, there is also room for improvement by decreasing the device area so as to reduce parasitic capacitance.

5. Temperature-dependent visible photoresponse and noise performance

Apart from room-temperature measurements, the photoresponse characterization was carried out at lower operating temperatures, so as to observe any potential enhancement in PD performance arising from the expected suppression of thermal carrier excitation. The top and back electrodes of the photodetector were wire-bonded onto a sample holder and mounted into a variable temperature closed cycle cryostat with fused silica windows for optical access [31]. The *I–V* characteristics of a 1 mm^2 active area photodetector comprising a W_{QD} = 200 nm QD layer on a *p*-type Si substrate were carried out in the dark and at a representative λ = 640 nm at 12 μW of incident power, from 300 K down to 100 K with a 50 K temperature step. The mean and standard deviation of two consecutive measurements sets are presented in Fig. 6, in which it is seen that the standard deviation of the current, represented with error bars, is negligible thus confirming robust devices with reproducible behavior. As seen in Fig. 6 (a), the dark current decreases by approximately one order of magnitude for every 50 K of temperature reduction as a direct consequence of reduced thermal generation of electron-hole pairs. This, in turn, increases the rectification ratio at symmetric voltages of –2 and 2 V from four (at 300 K) to seven orders of magnitude (at 100 K). The photoresponse, presented in Fig. 6 (b), exhibits a considerable decrease at low and intermediate reverse voltages, which is attributed to weaker phonon-assisted tunneling at lower temperatures. However, the measured total current

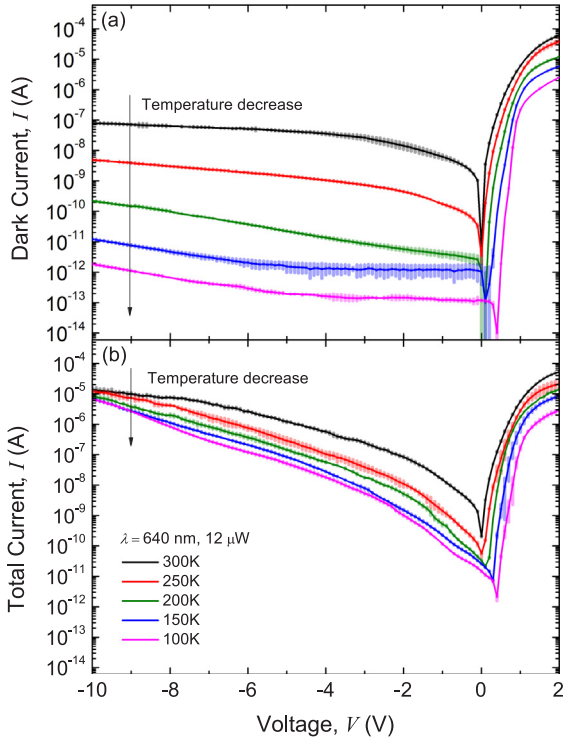

Fig. 6. *I–V* curves vs. temperature in the 100–300 K range of a 1 mm^2 photodetector (a) in the dark and (b) under illumination at 640 nm wavelength for 12 μW of incident power. Dark current decreases approximately one order of magnitude per 50 K as a consequence of reduced thermal generation of electron-hole pairs, whereas the current under illumination slightly decreases as a result of suppressed phonon-assisted tunneling, stemming from decreased phonon densities at lower temperatures. The error bars represent the standard deviation from the mean of two consecutive measurement sets, confirming reproducible photodetector performance.

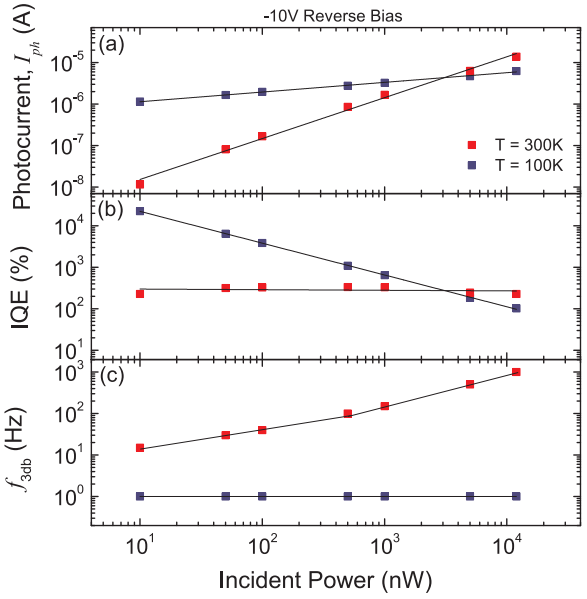

Fig. 7. Experimentally measured dependence of (a) photocurrent, (b) IQE and (c) 3 dB frequency response of the photodetector circuit on incident optical power ranging from 10 nW to 12 μW at −10 V reverse bias for operating temperatures of 300 and 100 K. At 300 K the photocurrent increases linearly with optical power, whereas at 100 K it exhibits a sublinear behavior resulting in higher IQE, due to longer hole lifetimes which also lead to a lower 3 dB frequency response at 100 K.

values at −10 V reverse bias converge to roughly the same value, leading to a far greater I_{ph}/I_d current ratio. As extracted from Fig. 6, at 300 K and −10 V of reverse bias the PD exhibits R_{sp} = 1.2 A/W, EQE = 226% and IQE = 228% calculated for experimentally measured reflectance R = 0.87% at λ = 640 nm. As for the 100 K case, despite the slight decrease in photocurrent, values of R_{sp} = 0.53 A/W, EQE = 102% and IQE = 103% were obtained, which in turn improve at lower illumination powers as discussed below.

The noise performance of a photodetector is characterized by the signal-to-noise ratio defined as SNR = I_{ph}/σ_n, where I_{ph} is the photocurrent and σ_n is the total current noise. Two main sources of current noise need to be considered: First is the photocurrent shot (Poisson) noise $\sigma_{ph}^2 = 2e(I_{ph}BG)$ associated with the discrete nature of photon-electron generation where e is the elementary charge, G is the internal gain (IQE) and B is the measurement bandwidth, i.e., half of the reciprocal of the measurement averaging time as imposed by the Nyquist sampling theorem $B = (2t_{avg})^{-1}$. The second source is the intrinsic thermal noise introduced by the detector circuit $\sigma_{th}^2 = (\sigma_j^2 + \sigma_d^2)$ where $\sigma_j^2 = 4kTB/R_L$ is the Johnson-Nyquist noise introduced by the thermal motion of charge within the load resistance R_L connected in series to the PD, k is the Boltzmann constant and $\sigma_d^2 = 2e(I_dBG)$ is the dark current shot noise [3]. The photocurrent and IQE dependence on various incident powers (P_{in}), ranging from 10 nW to 12 μW, measured for T = 300 and 100 K are summarized in Fig. 7 at −10 V reverse bias for a 1 mm^2 area PD with W_{QD} = 200 nm using a R_L = 15 kΩ resistor. At 300 K, I_{ph} increases linearly so IQE remains approximately constant. On the other hand, at 100 K the photocurrent shows a much weaker sublinear power dependence, therefore leading to a growing difference compared to 300 K as P_{in} is lowered, see Fig. 7 (a). The mechanism responsible for this trend is the following: At 100 K the number of available percolation paths within the QD layer through which electrons can tunnel reduces as a consequence of weaker phonon-assisted tunneling, resulting in longer hole lifetimes. Therefore, the photocurrent tends to saturate at lower incident powers compared to 300 K. This saturating trend of the photocurrent and the longer trapped charge lifetimes lead to strongly enhanced IQE with values in excess of 22000% as is shown in Fig. 7 (b). Additionally, the detector's electrical 3 dB frequency response (f_{3dB}) was also measured via frequency-dependent roll-off measurements of the voltage across the load resistor using digital modulation of the laser for both temperature values. As seen in Fig. 7 (c), at 300 K the frequency response increases sublinearly with incident optical power, as the conductivity of the PD increases, leading to a smaller total series resistance, thus a smaller $\mathscr{R}$C time constant, reaching a maximum of 1 kHz. This value agrees with the 3 dB bandwidth of 2 kHz measured for a 0.5 mm^2 area detector, possessing a ~ 50% smaller $\mathscr{R}$C constant. We point out that the smaller bandwidth values obtained here compared to the ones presented in Section 4 are due to a non-optimized device structure and measurement conditions, as larger W_{QD}, R_L and lower incident power were used here. At T = 100 K, the frequency response is dramatically suppressed and remains around 1 Hz throughout the incident power range, an effect also attributed to the longer charge trapping and hopping times within the QD matrix. Based on these findings, the dependence of the two sources of noise on incident power were calculated (see [31] for details), which makes it possible to estimate the respective SNR for the 300 and 100 K operating temperature cases. As observed in Fig. 8, in the low-power regime of P_{in} = 10 nW, SNR increases with decreasing temperature with values from 2 × 10^4 (at 300 K) to 2 × 10^5 (at 100 K), whereas the same maximum of 7 × 10^6 is observed at 12 μW for both temperatures. This is a direct result of the photocurrent (see Fig. 7) and photocurrent shot-noise behavior (see [31]) and is evidence that the photodetector benefits from 100 K operation mostly in the lower incident power regime.

Another important figure of merit to characterize the detector performance is the specific detectivity $D^* = (A)^{1/2}/$ NEP, where A is the photodetector area and NEP is the noise-equivalent-power normalized

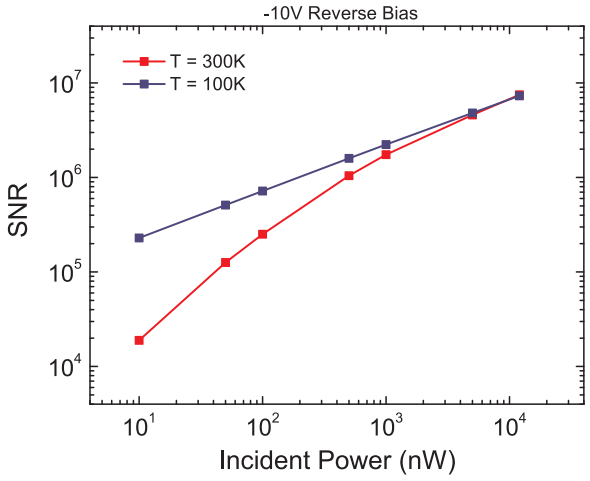

Fig. 8. SNR dependence on incident optical power at reverse bias of −10 V for operating temperatures of 300 and 100 K, showing up to an order of magnitude improvement in the low-power regime at 10 nW when the PD is cooled to 100 K.

by the measurement bandwidth B. Physically, NEP is a measure of the minimum optical power detectable by a photodetector, i.e., it is the power needed to generate a signal equal to the detector's intrinsic thermal noise floor, σ_{th}, resulting in SNR = 1, i.e., $I_{ph} = \sigma_{th}$, for a measurement bandwidth B of 1 Hz, i.e., a measurement time of 0.5 s. This implies that NEP $= \sigma_{th}/(R_{sp}\sqrt{B})$. Given that all measurements were carried out in a 1.6 s averaging time window (B = 0.3 Hz), this yielded NEP $= 9.6 \times 10^{-13}\ \mathrm{W}/\sqrt{Hz}$ and thus $D^* = 1.2 \times 10^{11}\ \mathrm{cmHz^{1/2}W^{-1}}$ at 300 K, a value that is competitive or even superior to various other material photodetectors reported for a similar wavelength at 300 K in the literature [32–39]. Following the same procedure for the 100 K case yielded NEP $= 5.3 \times 10^{-15}\ \mathrm{W}/\sqrt{Hz}$ and thus $D^* = 2 \times 10^{13}\ \mathrm{cmHz^{1/2}W^{-1}}$ which represents a two orders of magnitude improvement. It is important to note that the D^* values reported above were calculated for R_{sp} corresponding to the lowest P_{in} = 10 nW value. This does not change the value of D^* for the 300 K case, where R_{sp} is approximately constant regardless of P_{in}. In contrast, at 100 K, R_{sp} increases dramatically in the low P_{in} regime, as demonstrated in Fig. 7, leading to a significantly lower NEP and thus greater D^*. The detectivity calculated for R_{sp} at the highest incident power of 12 μW is approximately the same for both 300 and 100 K cases, meaning that the detector's noise performance only benefits from operating at 100 K in the low P_{in} regime, as is also evident in Fig. 8.

6. Temperature-dependent near-IR photoresponse and noise performance

Since the Si substrate is practically transparent to incident light above 1100 nm at 300 K, only electron-hole excitation in the Ge QDs themselves can significantly contribute to the photocurrent and thus the photoresponse at near-IR excitation is quite weak. In order to study the near-IR photoresponse, a NKT SuperK super-continuum laser was utilized as an illumination source, together with narrow bandpass filters (FWHM ~ 10 nm) with center wavelengths of 1100, 1300, 1400 and 1550 nm intercepting the beam, to pick up the desired wavelength. At 300 K the photoresponse in the near-IR was swamped by the dark current, however cooling the PD below 200 K produced a photocurrent approximately three orders of magnitude higher than the dark current at 1100 nm and up to two orders of magnitude higher than the dark current in the 1300–1550 nm range, at P_{in} = 12 μW and −10 V of bias. This produced weak $R_{sp} \leq 1$ mA/W in the aforementioned wavelength range (see [31] for details). Since such values are considerably low, in order to magnify the PDs' room-temperature near-IR photoresponse and

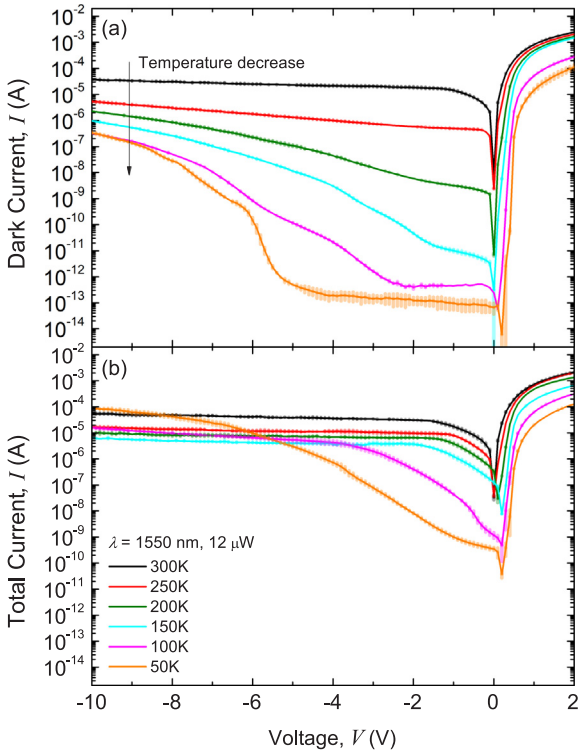

Fig. 9. I–V characteristics of a 1.5 $\mathrm{mm^2}$ PD in the dark (a) and under illumination of λ = 1550 nm at 12 μW of incident power (b), as a function of operating temperature in the 50–300 K range.

most importantly at the λ = 1550 nm telecommunication wavelength, devices were fabricated by depositing the Ge QD containing SiO_2 matrix on Ge rather than Si substrates following the same fabrication procedure as the one described in Section 2. Devices with active areas equal to 1.5 $\mathrm{mm^2}$ defined by photolithography, comprising a W_{QD} = 160 nm QD layer and with a 100 nm-thick IZO layer as a top contact were realized.

I–V characterization of the photodetector was carried out in the dark and at λ = 1550 nm for 12 μW of incident power, from 300 K down to 50 K with a 50 K temperature step in order to suppress the considerably higher dark current due the smaller bandgap of the Ge substrate. The mean and standard deviation (shown by error bars) of two consecutive measurements sets are presented in Fig. 9, where the small error bars confirm reproducible and robust device behavior. As seen in Fig. 9 (a) the dark current decreases with temperature which in turn increases the rectification ratio at symmetric voltages of –2 and 2 V from two (at 300 K) to nine orders of magnitude (at 50 K). The photoresponse, presented in Fig. 9 (b), exhibits a considerable decrease at low reverse voltages for 50 and 100 K, which is attributed to weaker phonon-assisted tunneling at lower temperatures. However, at higher reverse voltages (greater than −8 V) and T = 50 K the photocurrent exceeds that at 300 K. This is attributed to the increase in carrier mobility in the Ge substrate as temperature drops [40]. What is more, the saturated behavior of the photocurrent for reverse bias in the –10 to −2 V range at operating temperatures of 150–300 K indicates that the PDs can be operated at much lower voltage with almost unchanged performance in this temperature range. Based on the $I(V)$ characterization presented in Fig. 9, the responsivity as a function of operating temperature and bias can be extracted yielding the following: For −10 V bias at 300 K, R_{sp} = 1.5 A/W, corresponding to EQE = 118% and IQE = 134% for an experimentally measured sample reflectance R = 12.17% at λ = 1550 nm, values which are higher than a commercial Ge photodiode measured at the same wavelength [41]. A maximum R_{sp} = 7.4 A/W, EQE = 590% and IQE = 672% are achieved

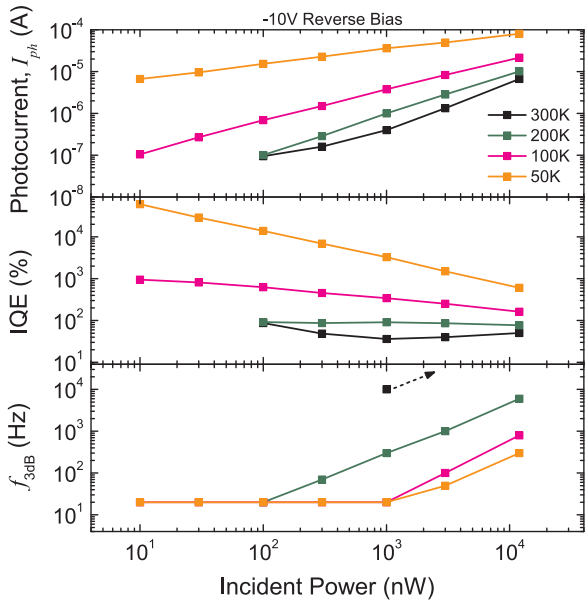

Fig. 10. Experimentally measured dependence of (a) photocurrent, (b) IQE and (c) 3 dB frequency response on incident optical power at $\lambda = 1550$ nm ranging from 10 nW to 12 μW at −10 V reverse bias for operating temperatures in the 50–300 K range. As temperature decreases the photocurrent becomes more sublinear resulting in higher IQE, which in turn increases with diminishing optical power resulting from a saturated QD charging process (see Section 5). At 300 K, $f_{3dB} = 10$ kHz for $P_{in} = 1$ μW, where dashed arrow indicates increasing f_{3dB} values with incident power. (Quantitative values not obtained due to limited range of chopper frequencies.) As temperature is lowered, f_{3dB} values respectively decrease.

at 50 K, due to increasing I_{ph} for temperatures below 150 K.

The dependence of the photocurrent, IQE and 3 dB bandwidth on P_{in} ranging 10 nW to 12 μW at $\lambda = 1550$ nm are presented in Fig. 10 for −10 V of reverse bias at various operation temperatures, namely 300, 200, 100 and 50 K, using $R_L = 15$ kΩ. We point out here that at temperatures of 300 and 200 K and $P_{in} = 10$ nW and 30 nW, photoresponse is not discernible within a standard deviation of two consecutive *I–V* measurements sets as the total current is dominated by the dark current. As can be observed in Fig. 10 (a), for T = 300 K the photocurrent exhibits linear behavior for $P_{in} > 1$ μW, becoming sublinear at lower values. This is due to the total current approaching the dark current, thus leading to negligible I_{ph}, which consequently plateaus as illumination power decreases far below 1 μW. Furthermore, for temperatures below 300 K the photocurrent becomes increasingly sublinear as a function of incident power. As is evident from Fig. 10 (b), this leads to IQE increasing as incident power is lowered, an effect that is magnified with decreasing temperature (as also demonstrated in Section 5 for visible excitation). Specifically, at 10 nW, IQE values of ~ 1000% are reached at 100 K and in excess of 60000% when further lowering the temperature to 50 K. The dependence of f_{3dB} on incident power for the various operating temperatures is presented in Fig. 10 (c). At 300 K and 1 μW of incident power $f_{3dB} = 10$ kHz. The room-temperature f_{3dB} further increases when $P_{in} > 1$ μW, however quantitative values were not obtained due to the limited range of chopper frequencies achievable. Photoresponse for $P_{in} < 1$ μW is not discernible so f_{3dB} is not provided. At 200 K, following a sublinear increase above 100 nW of incident power, f_{3dB} reaches a maximum of 6 kHz at 12 μW. As operating temperature is decreased f_{3dB} also decreases in accordance with the results presented in Section 5. At 100 K, as well as 50 K, f_{3dB} increases sublinearly above 1 μW with maximum values falling to 800 Hz and 300 Hz respectively, whereas it remains around or below 20 Hz at lower powers. It is worth noting that even though these bandwidth values are significantly smaller than the ones obtained for visible

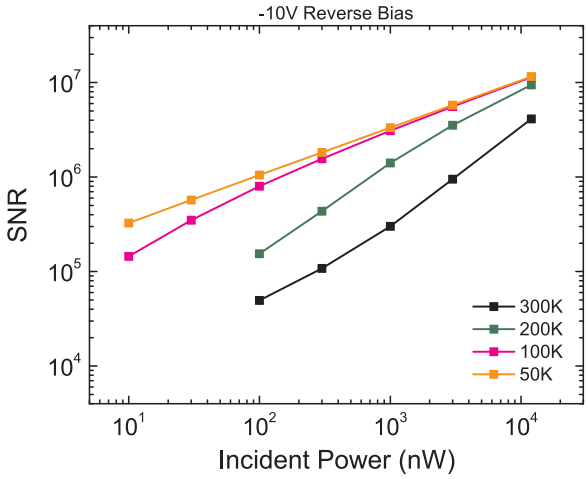

Fig. 11. SNR dependence on incident power and operating temperature, at −10 V of reverse bias, showing an increasing trend as temperature is decreased, especially at lower incident powers, where the enhancement is most prominent.

excitation presented in Section 4, higher values can be achieved in devices with thinner W_{QD} and by minimizing parasitic capacitance and R_L. Knowledge of the photocurrent and IQE dependence on P_{in} and temperature provides the respective SNR dependence shown in Fig. 11. The maximum room-temperature SNR is 4×10^6 at 12 μW of incident power. For operation below 200 K the SNR at 12 μW remains relatively unchanged at 10^7, whereas for low incident power of 10 nW, it is dramatically increased from zero at 300 K (because of the total current being swamped by the dark current) to 1.5×10^5 at 100 K, further increasing at 50 K. The specific detectivity (D^*) dependence on incident power and temperature, is presented in Fig. 12. When temperature is lowered, D^* increases as a direct consequence of decreasing thermal noise and increasing R_{sp}. Specifically, as a function of incident power, D^* remains approximately constant at 300 K with a value $\sim 3 \times 10^{10}$ cmHz$^{1/2}$W^{-1} which is competitive to Ge based photodetectors reported for a similar wavelength and temperature in the literature [42,43], whereas at 200 K $D^* \sim 1.1 \times 10^{11}$ cmHz$^{1/2}$W^{-1}. In both cases the value is approximately constant because of the approximately unchanging IQE. On the other hand for T = 100 K and 50 K, D^* increases with decreasing incident power as a direct consequence of growing R_{sp} (see Fig. 10 (a) and (b)) and reaches a

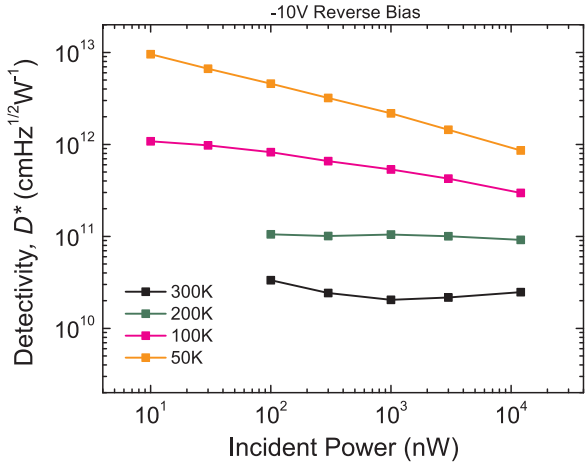

Fig. 12. Specific detectivity (D^*) dependence on incident power and operating temperature, at −10 V of reverse bias with values remaining approximately constant for temperatures of 300 and 200 K, however showing a climbing trend as a direct consequence of increasing IQE at lower incident powers for temperatures below 200 K (see Fig. 10).

maximum of 1.1×10^{12} cmHz$^{1/2}$W^{-1} for 100 K and 10^{13} cmHz$^{1/2}$W^{-1} for 50 K, at the lowest $P_{in} = 10$ nW optical power value.

7. Summary

To summarize, we have provided a review of our work on Ge QD photodetectors fabricated on Si and Ge substrates that exhibit superior room-temperature responsivity in the visible and near-IR compared to commercial Si or Ge photodiodes as a consequence of high internal photoconductive gain. Specifically, devices grown on Si substrates showed a broad and uniform spectral photoresponse with R_{sp} above 1 A/W over the entire $\lambda = 550$–1000 nm range at -10 V bias, with a peak responsivity of 4 A/W at 900 nm corresponding to IQE = 700%. Photodetectors fabricated on Ge substrates showed room-temperature $R_{sp} = 1.5$ A/W corresponding to IQE = 134% for the $\lambda = 1550$ nm telecommunications wavelength at -10 V bias. As for their frequency response, at room-temperature operation 3 dB bandwidths up to 10 MHz were achieved at $\lambda = 670$ nm for optimized conditions, i.e. thinning down the QD layer and minimizing the load resistance R_L. At $\lambda = 1550$ nm, $f_{3dB} = 10$ kHz was obtained, which can be equivalently enhanced by optimizing the device structure and measurement conditions. Noise performance characterization for PDs on Si substrates and visible excitation of 640 nm showed maximum room-temperature SNR of 7×10^6 at $P_{in} = 12$ μW, whereas for devices on Ge substrates a maximum SNR of 4×10^6 was reported at $\lambda = 1550$ nm for the same P_{in}. By lowering the operation temperature, it was shown that the noise performance at both 640 and 1550 nm is strongly enhanced especially at lower P_{in}. For PDs on Si substrates, SNR at 10 nW was increased from 2×10^4 (at 300 K) to 2×10^5 (at 100 K), thus showing an order of magnitude improvement due to photoconductive gain over 22000% resulting from saturation of the QD charging process at low temperature. For $\lambda = 1550$ nm at 300 K and $P_{in} = 10$ nW, the PD showed no photoresponse, however lowering the temperature to 100 K led to SNR = 1.5×10^5, increasing even further to 3×10^5 at 50 K, stemming from photoconductive gain values over 60000%. Finally, devices on Si substrates exhibited room-temperature specific detectivity of $D^* = 1.2 \times 10^{11}$ cmHz$^{1/2}$W^{-1} at $\lambda = 640$ nm achieving two orders of magnitude increase up to $D^* = 2 \times 10^{13}$ cmHz$^{1/2}$W^{-1} when lowering the temperature to 100 K, at $P_{in} = 10$ nW. As for PDs on Ge substrates, room-temperature detectivity of 3×10^{10} cmHz$^{1/2}$W^{-1} was achieved at $\lambda = 1550$ nm, improving to 1.1×10^{12} cmHz$^{1/2}$W^{-1} at 100 K and 10^{13} cmHz$^{1/2}$W^{-1} at 50 K, for $P_{in} = 10$ nW. Based on the figures of merit presented above, our Ge QD photodetectors prove to be competitive or even superior to commercial Si or Ge photodiodes as well as other material PDs reported in the literature for detection in the visible and near-IR, (see Table S1 [44]) as long as their time response is further enhanced by optimizing the QD-containing layer.

Acknowledgements

This work was supported by the National Science Foundation under grants DMR–1203186, CMMI–1530547, as well as Brown University seed award GR300030.

Appendix A. Supplementary data

Supplementary data associated with this article can be found in the online version at http://dx.doi.org/10.1016/j.mssp.2018.03.024.

References

[1] J.-M. Shieh, W.-C. Yu, J.Y. Huang, C.-K. Wang, B.-T. Dai, H.-Y. Jhan, C.-W. Hsu, H.-C. Kuo, F.-L. Yang, C.-L. Pan, Near-infrared silicon quantum dots metal-oxide-semiconductor field-effect transistor photodetector, Appl. Phys. Lett. 94 (2009) 241108.
[2] J.-M. Shieh, Y.-F. Lai, W.-X. Ni, H.-C. Kuo, C.-Y. Fang, J.Y. Huang, C.-L. Pan, Enhanced photoresponse of a metal-oxide-semiconductor photodetector with silicon nanocrystals embedded in the oxide layer, Appl. Phys. Lett. 90 (2007) 051105.
[3] F. Träger, Handbook of Lasers and Optics, Springer, 2012.
[4] B.-C. Hsu, S. Chang, T.-C. Chen, P.-S. Kuo, P. Chen, Z. Pei, C. Liu, A high efficient 820 nm MOSGe quantum dot photodetector, IEEE Electron Device Lett. 24 (2003) 318–320.
[5] S. Tzeng, P. Li, Enhanced 400–600 nm photoresponsivity of metal-oxide-semiconductor diodes with multi-stack germanium quantum dots, Nanotechnology 19 (2008) 235203.
[6] S. Cosentino, E. Barbagiovanni, I. Crupi, M. Miritello, G. Nicotra, C. Spinella, D. Pacifici, S. Mirabella, A. Terrasi, Size dependent light absorption modulation and enhanced carrier transport in germanium quantum dots devices, Sol. Energy Mater. Sol. Cells 135 (2015) 22–28.
[7] G. Konstantatos, E.H. Sargent, Nanostructured materials for photon detection, Nat. Nanotechnol. 5 (2010) 391–400.
[8] J.P. Clifford, G. Konstantatos, K.W. Johnston, S. Hoogland, L. Levina, E.H. Sargent, Fast, sensitive and spectrally tuneable colloidal-quantum-dot photodetectors, Nat. Nanotechnol. 4 (2009) 40–44.
[9] G. Konstantatos, I. Howard, A. Fischer, S. Hoogland, J. Clifford, E. Klem, L. Levina, E.H. Sargent, Ultrasensitive solution-cast quantum dot photodetectors, Nature 442 (2006) 180–183.
[10] H. Lim, S. Tsao, W. Zhang, M. Razeghi, High-performance InAs quantum-dot infrared photodetectors grown on InP substrate operating at room temperature, Appl. Phys. Lett. 90 (2007) 131112.
[11] B.S. Passmore, J. Wu, M. Manasreh, G. Salamo, Dual broadband photodetector based on interband and intersubband transitions in InAs quantum dots embedded in graded InGaAs quantum wells, Appl. Phys. Lett. 91 (2007) 233508.
[12] J.C. Campbell, A. Madhukar, Quantum-dot infrared photodetectors, Proc. IEEE 95 (2007) 1815–1827.
[13] S. Chakrabarti, S. Adhikary, N. Halder, Y. Aytac, A. Perera, High-performance, long-wave (~ 10.2 um) InGaAs/GaAs quantum dot infrared photodetector with quaternary In $_{0.21}$ Al $_{0.21}$ Ga $_{0.58}$ As capping, Appl. Phys. Lett. 99 (2011) 181102.
[14] X. Lu, J. Vaillancourt, M.J. Meisner, Temperature-dependent photoresponsivity and high-temperature (190 K) operation of a quantum dot infrared photodetector, Appl. Phys. Lett. 91 (2007) 051115.
[15] E.-T. Kim, A. Madhukar, Z. Ye, J.C. Campbell, High detectivity InAs quantum dot infrared photodetectors, Appl. Phys. Lett. 84 (2004) 3277–3279.
[16] B. Zhang, S. Shrestha, M. Green, G. Conibeer, Size controlled synthesis of Ge nanocrystals in SiO_2 at temperatures below 400 °C using magnetron sputtering, Appl. Phys. Lett. 96 (2010) 261901.
[17] D. Pacifici, E. Moreira, G. Franzo, V. Martorino, F. Priolo, F. Iacona, Defect production and annealing in ion-irradiated Si nanocrystals, Phys. Rev. B 65 (2002) 144109.
[18] S. Cosentino, S. Mirabella, M. Miritello, G. Nicotra, R.L. Savio, F. Simone, C. Spinella, A. Terrasi, The role of the surfaces in the photon absorption in Ge nanoclusters embedded in silica, Nanoscale Res. Lett. 6 (2011) 135.
[19] M. Fujii, O. Mamezaki, S. Hayashi, K. Yamamoto, Current transport properties of SiO_2 films containing Ge nanocrystals, J. Appl. Phys. 83 (1998) 1507–1512.
[20] Y. Maeda, Visible photoluminescence from nanocrystallite Ge embedded in a glassy SiO_2 matrix: evidence in support of the quantum-confinement mechanism, Phys. Rev. B 51 (1995) 1658.
[21] S. Cosentino, S. Mirabella, P. Liu, S.T. Le, M. Miritello, S. Lee, I. Crupi, G. Nicotra, C. Spinella, D. Paine, et al., Role of Ge nanoclusters in the performance of photodetectors compatible with Si technology, Thin Solid Films 548 (2013) 551–555.
[22] S. Cosentino, P. Liu, S.T. Le, S. Lee, D. Paine, A. Zaslavsky, D. Pacifici, S. Mirabella, M. Miritello, I. Crupi, et al., High-efficiency silicon-compatible photodetectors based on Ge quantum dots, Appl. Phys. Lett. 98 (2011) 221107.
[23] S. Siontas, P. Liu, A. Zaslavsky, D. Pacifici, Noise performance of high-efficiency germanium quantum dot photodetectors, Appl. Phys. Lett. 109 (2016) 053508.
[24] C.Y. Chien, W.T. Lai, Y.J. Chang, C.C. Wang, M.H. Kuo, P.W. Li, Size tunable Ge quantum dots for near-ultraviolet to near-infrared photosensing with high figures of merit, Nanoscale 6 (2014) 5303–5308.
[25] P. Martyniuk, A. Rogalski, Quantum-dot infrared photodetectors: status and outlook, Prog. Quantum Electron. 32 (2008) 89–120.
[26] H. Schneider, H.C. Liu, Quantum Well Infrared Photodetectors, Springer, 2007.
[27] P. Liu, S. Cosentino, S.T. Le, S. Lee, D. Paine, A. Zaslavsky, D. Pacifici, S. Mirabella, M. Miritello, I. Crupi, et al., Transient photoresponse and incident power dependence of high-efficiency germanium quantum dot photodetectors, J. Appl. Phys. 112 (2012) 083103.
[28] M. Martens, J. Schlegel, P. Vogt, F. Brunner, R. Lossy, J. Würfl, M. Weyers, M. Kneissl, High gain ultraviolet photodetectors based on AlGaN/GaN heterostructures for optical switching, Appl. Phys. Lett. 98 (2011) 211114.
[29] S.H. Im, J.A. Chang, S.W. Kim, S.-W. Kim, S.I. Seok, Near-infrared photodetection based on PbS colloidal quantum dots/organic hole conductor, Org. Electron. 11 (2010) 696–699.
[30] L. Chu, A. Zrenner, D. Bougeard, M. Bichler, G. Abstreiter, A quantum dot infrared photodetector with lateral carrier transport, Phys. E: Low.-Dimens. Syst. Nanostruct. 13 (2002) 301–304.
[31] S. Siontas, D. Li, P. Liu, S. Aujla, A. Zaslavsky, D. Pacifici, Low-temperature operation of high-efficiency germanium quantum dot photodetectors in the visible and near infrared, Phys. Status Solidi (a) (2017) 1700453.
[32] J. Yao, J. Shao, Y. Wang, Z. Zhao, G. Yang, Ultra-broadband and high response of the Bi_2Te_3-Si heterojunction and its application as a photodetector at room temperature in harsh working environments, Nanoscale 7 (2015) 12535–12541.
[33] L. Dou, Y.M. Yang, J. You, Z. Hong, W.-H. Chang, G. Li, Y. Yang, Solution-processed hybrid perovskite photodetectors with high detectivity, Nat. Commun. 5 (2014).

[34] J. Qi, L. Ni, D. Yang, X. Zhou, W. Qiao, M. Li, D. Ma, Z.Y. Wang, Panchromatic small molecules for UV–Vis–NIR photodetectors with high detectivity, J. Mater. Chem. C 2 (2014) 2431–2438.
[35] M.S. Choi, D. Qu, D. Lee, X. Liu, K. Watanabe, T. Taniguchi, W.J. Yoo, Lateral MoS_2 p-n junction formed by chemical doping for use in high-performance optoelectronics, ACS Nano 8 (2014) 9332–9340.
[36] D.-S. Tsai, K.-K. Liu, D.-H. Lien, M.-L. Tsai, C.-F. Kang, C.-A. Lin, L.-J. Li, J.-H. He, Few-layer MoS_2 with high broadband photogain and fast optical switching for use in harsh environments, ACS Nano 7 (2013) 3905–3911.
[37] Z. Liu, T. Luo, B. Liang, G. Chen, G. Yu, X. Xie, D. Chen, G. Shen, High-detectivity InAs nanowire photodetectors with spectral response from ultraviolet to near-infrared, Nano Res. 6 (2013) 775–783.
[38] M. Sofos, J. Goldberger, D.A. Stone, J.E. Allen, Q. Ma, D.J. Herman, W.-W. Tsai, L.J. Lauhon, S.I. Stupp, A synergistic assembly of nanoscale lamellar photoconductor hybrids, Nat. Mater. 8 (2009) 68–75.
[39] M. Razeghi, A. Rogalski, Semiconductor ultraviolet detectors, J. Appl. Phys. 79 (1996) 7433–7473.
[40] P. Debye, E.M. Conwell, Electrical properties of n-type germanium, Phys. Rev. 93 (1954) 693.
[41] Biased Ge detectors 800–1800 nm ⟨https://www.thorlabs.com⟩.
[42] N. Yahyaoui, N. Sfina, J. Lazzari, A. Bournel, M. Said, Performance evaluation of high-detectivity p-i-n infrared photodetector based on compressively-strained $Ge_{0.964}Sn_{0.036}$/Ge multiple quantum wells by quantum modelling, Semicond. Sci. Technol. 30 (2015) 085016.
[43] L.-H. Zeng, M.-Z. Wang, H. Hu, B. Nie, Y.-Q. Yu, C.-Y. Wu, L. Wang, J.-G. Hu, C. Xie, F.-X. Liang, et al., Monolayer graphene/germanium Schottky junction as high-performance self-driven infrared light photodetector, ACS Appl. Mater. Interfaces 5 (2013) 9362–9366.
[44] See supplementary material at: 10.1016/j.mssp.2018.03.024 for a table comparing the performance and figures of merit of several photodetectors based on published data.